Title

Anisotropic electronic state via spontaneous phase separation in strained vanadium dioxide films.

Journal

Physical review letters, 111(9)

ISSN

0031-9007

Authors

Liu, MK
Wagner, M
Abreu, E
et al.

Publication Date

2013-08-01

DOI

10.1103/physrevlett.111.096602

Peer reviewed

Anisotropic Electronic State via Spontaneous Phase Separation in Strained Vanadium Dioxide Films

Article *in* Physical Review Letters · August 2013
DOI: 10.1103/PhysRevLett.111.096602 · Source: PubMed

Anisotropic Electronic State via Spontaneous Phase Separation in Strained Vanadium Dioxide Films

M. K. Liu,[1] M. Wagner,[1] E. Abreu,[2] S. Kittiwatanakul,[3] A. McLeod,[1] Z. Fei,[1] M. Goldflam,[1] S. Dai,[1] M. M. Fogler,[1] J. Lu,[4] S. A. Wolf,[3,4] R. D. Averitt,[2] and D. N. Basov[1,*]

[1]*Department of Physics, The University of California at San Diego, La Jolla, California 92093, USA*
[2]*Department of Physics, Boston University, Boston, Massachusetts 02215, USA*
[3]*Department of Physics, University of Virginia, Charlottesville, Virginia 22904, USA*
[4]*Department of Materials Science and Engineering, University of Virginia, Charlottesville, Virginia 22904, USA*

(Received 11 May 2013; published 29 August 2013)

We resolved the enigma of anisotropic electronic transport in strained vanadium dioxide (VO_2) films by inquiring into the role that strain plays in the nanoscale phase separation in the vicinity of the insulator-to-metal transition. The root source of the anisotropy was visualized as the formation of a peculiar unidirectional stripe state which accompanies the phase transition. Furthermore, nanoscale infrared spectroscopy unveils distinct facets of electron-lattice interplay at three different stages of the phase transition. These stages include the initial formation of sparse nonpercolating metallic domains without noticeable involvement of the lattice followed by an electron-lattice coupled anisotropic stripe state close to percolation which ultimately evolves into a nearly isotropic rutile metallic phase. Our results provide a unique mesoscopic perspective for the tunable macroscopic phenomena in strained metal oxide films.

DOI: 10.1103/PhysRevLett.111.096602 PACS numbers: 72.80.Ga, 73.22.−f, 73.23.−b, 78.20.−e

Strain can cause striking new physics in materials with examples that include an increase of the superconducting transition temperature [1], an enhancement of ferroelectric polarization [2], and even giant pseudomagnetic fields in excess of 300 Tesla [3]. Spontaneous formation of polydomains by strain can generate new macroscopic order [4,5], leading to the coexistence of multiple constituent phases in complex materials [6–8]. Transition metal oxides serve as a test bed to investigate strain and phase separation, clarifying the roles of these effects in technologically important phenomena including superconductivity, magnetoresistance and electro-opitcal switching. With broadband infrared near-field microscopy, we reveal the formation of unidirectional conducting stripes in strained VO_2 films, linked to dramatic conductivity anisotropy and modification of the metal-insulator transition (MIT) temperature T_c.

The MIT in vanadium dioxide (VO_2) at 340 K accompanied by a transition from a low temperature monoclinic (M) phase to a high temperature rutile (R) phase has remained a topic of intense interest since the 1950s [9,10]. One poorly understood aspect of VO_2 physics is the anisotropy of the transition temperature (T_c) and dc conductivity in the vicinity of the MIT. In different forms of vanadium dioxide (VO_2) crystals or films, the degree of electronic anisotropy can range from a factor of 10 to 50 to vanishingly small without any obvious reasons. Such anisotropy was noticed early on [11] but became increasingly apparent with the recent advent of highly ordered crystalline films grown on TiO_2 substrates [12,13]. This is inconsistent with the structure of VO_2 in any of its known crystalline phases [14]. Furthermore, this unusual anisotropic state is predicted by neither the Mott nor Peierls theories of the MIT, the two leading scenarios invoked to explain the phase transition physics on the basis of electronic correlations and structural transformations, respectively [15,16]. Because meso- and nanoscale phase separation is commonplace in the physics of VO_2, addressing the anisotropy enigma calls for an exploration of structural and electronic properties at the nanoscale.

Despite rapid progress in the development of scanning probe techniques [17–19], simultaneously probing nanoscale variations of electronic and structural properties over large scanning areas has remained a challenging task. To meet this need, in this work, we employ scattering-type scanning near-field optical microscopy (s-SNOM). Based on an atomic force microscope (AFM), the s-SNOM detects tip-scattered infrared (IR) signals which render local information about the optical properties of the sample surface [17,19]. Signals S_n demodulated at integer harmonics $n = 2$, 3, 4 of the fundamental tip tapping frequency are recorded to isolate the genuine near-field contribution to the infrared signal and eliminate additive background artifacts (see the Supplemental Material [20] for further details). Our particular s-SNOM arrangement enables topographic mapping, near-field imaging, and nano-Fourier-transform IR spectroscopy (nano-FTIR) with a spatial resolution down to ~20 nm carried out over a broad range of mid-IR frequencies (~650 to ~2400 cm^{-1}) [21,22]. In addition, we applied a high repetition rate (40 MHz) near-IR (~1.56 μm) pump beam focused to a 20 μm spot beneath the AFM tip to initiate the MIT in VO_2. Because of the long recovery time of our VO_2 samples (> 25 ns) in comparison with the laser

repetition rate, the pump beam provides an ultrastable local thermal environment without transient dynamics. Thus, by performing direct pump heating, the AFM measurements are much more stable and the images are sharper at elevated temperatures. With this experimental setup, we observed unidirectional electronic and structural domains in VO_2, corresponding to real-space signatures of the anisotropic state in the vicinity of the MIT. We identified three distinct stages of the MIT in the temperature range 320–380 K, revealing previously unnoticed aspects of the interplay between structural and electronic transformations in the course of the transition [Fig. 1(a)].

Figure 1(b) displays the temperature-dependent THz conductivity (σ_{THz}) of our 300 nm VO_2 film on the $[110]_R$ TiO_2 substrate, measured by Terahertz time domain spectroscopy (see the Supplemental Material [20] for further details). σ_{THz} along two different axes ($[1\bar{1}0]_R$ and $[001]_R$) was obtained by rotating the film 90° and probing the free-carrier response by polarized THz transmission. The conductivity increase along the $[001]_R$ axis begins at $T_{\parallel} \simeq 360$ K and proceeds with a sharp and narrow hysteresis. Along the $[1\bar{1}0]_R$ axis, the increase in conductivity onsets at a lower temperature ($T_{\perp} \simeq 320$ K) and the transition trace is unexpectedly broad, with complete metallicity not attained until ~380 K. Therefore, VO_2 films on $[110]_R$ TiO_2 exhibit a dramatically anisotropic conductivity in the vicinity of the phase transition. This behavior has not been observed in polycrystalline samples, such as VO_2 films grown on a sapphire substrate, confirming the key role of uniaxial strain. The apparent increase in T_c along the c_R axis of VO_2 on TiO_2 films has previously been attributed to strain-induced modulation of the electronic bandwidth [15,23] without considering spatial inhomogeneity. As we will show below, in order to understand the data in Fig. 1(b), the underlying physics of strained VO_2 films must be amended by taking proper account of a dominant role of unidirectional phase separation.

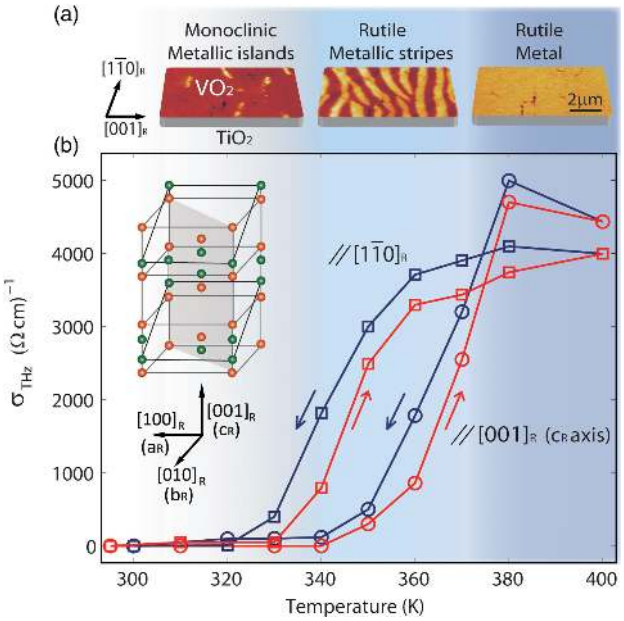

FIG. 1 (color online). (a) Near-field IR images illustrating three distinct stages of the insulator-to-metal phase transition as described in the text. (b) Temperature-dependent THz conductivity (σ_{THz}) along the $[1\bar{1}0]_R$ axis (squares) and along the $[001]_R$ axis (circles). Red (gray) and blue (black) arrows reflect directions of temperature change. Inset: crystal structure of VO_2 in low temperature monoclinic [green (black) spheres] and high temperature rutile [orange (gray) spheres] phases. The shaded plane coincides with the surface of our sample film.

Figure 2 presents our central findings: infrared near-field and AFM images of the 300 nm VO_2 film on $[110]_R$ TiO_2. The first and second rows of Fig. 2 display infrared near-field (S_3) and AFM topography images, respectively. Experiments were performed at room temperature, and the optical pump power was controlled by a neutral density filter (0–25 mW). As shown in the first row in Fig. 2, a highly stripe-ordered pattern with unidirectional domains running along $[1\bar{1}0]_R$ was observed by near-field imaging. The density and width of these stripes gradually increase with increasing pump intensity. Since higher local optical conductivities yield stronger infrared near-field signal (see the Supplemental Material [20] for further details), these near-field images clearly reveal the pump-induced formation of submicron wide metallic stripes. Essentially identical patterns were observed in temperature-dependent imaging experiments (Fig. 2, third row). Comparing light- and temperature-induced changes in our films, we infer that 16 mW of pump power corresponds with a temperature of ~326 K, whereas 22 mW corresponds with ~345 K.

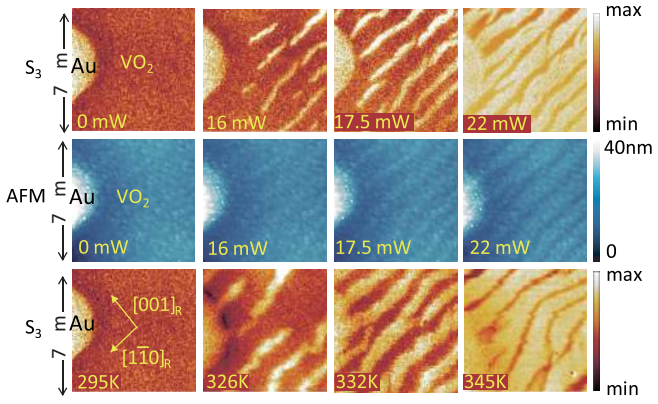

FIG. 2 (color online). Top row: IR scattering amplitude S_3 recorded at distinct power levels of the pump laser. Middle row: sample topography (AFM) for the images displayed in the top row. Bottom row: S_3 images recorded at distinct temperatures. The center frequency of the probe beam used here is ~1100 cm^{-1}. The near-field signal in all images is normalized to that from a 50 nm gold film (middle left of each image). Temperature-dependent Raman experiments (not shown) indicate that the monoclinic (M) and rutile (R) phases are coexistent in the temperature range 325–345 K.

AFM images acquired simultaneously with the pump-induced near-field data also show periodic stripe-ordered topographic features (Fig. 2, second row), as will be discussed in detail below. Temperature-dependent Raman experiments (spatially averaged over 2 μm due to limited optical resolution, not shown) confirmed the coexistence of monoclinic and rutile phases, as observed previously in VO_2 nanobeams and nanoplatelets [24–27]. Film thickness-dependent studies were also performed to demonstrate the ubiquity of the stripe order in strained VO_2 films, significantly expanding experimental insights into the stripe state, which until now was only observed in the geometrically confined nanoribbons (see the Supplemental Material [20]).

Figure 2 reveals that the metallic stripes align preferentially along the $[1\bar{1}0]_R$ axis, thus opening conductive paths along this direction. In contrast, conductivity along the $[001]_R$ axis is hindered by the intervening insulating domains. Thus, infrared near-field images link the anisotropic conductivity observed by THz measurements (Fig. 1) with a novel mesoscale, unidirectional electronic phase separation (Fig. 2).

The observed transformations in film morphology near the MIT are an entirely novel outcome of our imaging experiments. Figure 3 compares images and corresponding line scans acquired under pump powers of 15 and 20 mW. Simultaneously acquired AFM topography and infrared near-field amplitude (S_3) are overlaid to highlight the degree of correlation between the two effects [Figs. 3(a) and 3(b)]. At the initial stage of the phase transition (15 mW, i.e., $T \sim 320$ K), enhancement in the infrared near-field signal shows the formation of sparse metallic nanodomains to be uncorrelated with film topography within our AFM resolution [Fig. 3(c)]. At a later stage

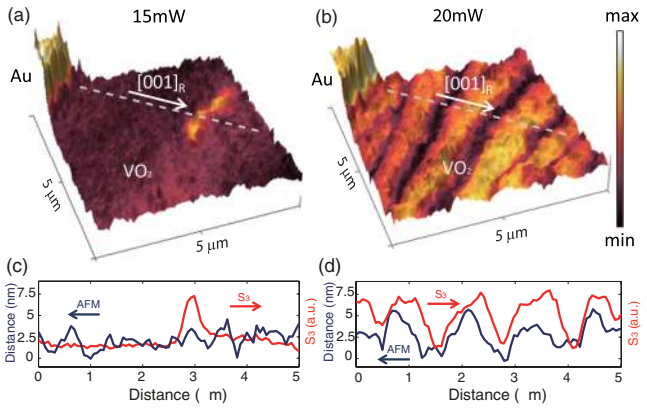

FIG. 3 (color online). (a),(b) The sample morphology (AFM) as a topographic map overlaid with the near-field scattering amplitude signal S_3 as given in the color scale. Corresponding line scans of AFM topography dark blue (black) curves and near-field amplitude red (gray) curves are shown in (c) and (d). Near-field signals are normalized to that from the 50 nm gold film at the upper left corners of (a) and (b).

(20 mW, i.e., $T \sim 340$ K), the density of metallic stripes increases and we observe an unmistakable correlation between infrared near-field amplitude and topographic features; the metallic stripes systematically coincide with height elevations of ~5 nm [Fig. 3(d)].

The correlation between infrared amplitude and topography observed at the advanced stages of the MIT is consistent with the notion of a structural transformation in VO_2 occurring within unidirectional stripes. In order to minimize the strain energy induced by interfacial lattice mismatch, the structural transition occurs in periodic domains oriented along $[1\bar{1}0]_R$, allowing part of the film to expand out of plane. It is well known that during the MIT, the rutile a_R (monoclinic b_m) axis expands by ~0.6% and the c_R (a_m) axis shrinks by as much as ~1% [28]. In our VO_2 films, topography elevations indicate an expansion of the a_R and b_R axes commensurate with the above expectations. Therefore, the periodic topographic stripes indicate a rutile-monoclinic-rutile structural variation accompanied by a corresponding anisotropy in electronic transport. The periodicity of the stripes decreases with decreasing film thickness, reflecting a competition between the domain interfacial energy and the elastic misfit energy (see the Supplemental Material [20] for further details).

To gain further insight into the interplay between electronic and structural properties across the MIT, we performed spatially resolved nano-FTIR experiments. Figure 4 presents spectra revealing the VO_2 phonon response at the initial stage of the MIT. After locating a

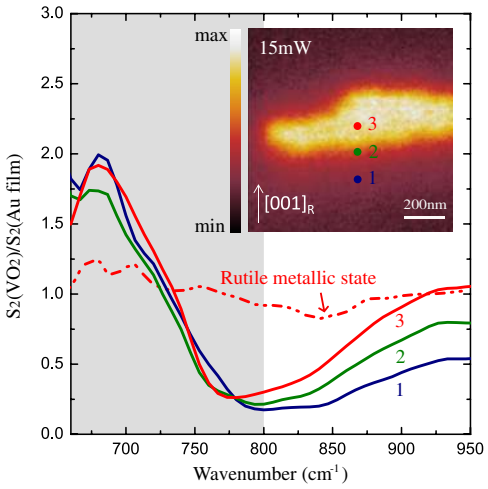

FIG. 4 (color online). Nano-FTIR spectra S_2 normalized to gold and recorded at different positions (1–3) indicated in the inset image of near-field amplitude. The phonon mode of the monoclinic phase of VO_2 at ~680 cm^{-1} can be clearly resolved at all locations 1–3. Note that this phonon peak persists even within the middle of the metallic stripe (3), suggesting a monoclinic metallic state. At higher pump power (20 mW), the monoclinic phonon response disappears at the center of the stripe, signaling a transition to the rutile metallic phase (dash-dotted red curve).

metallic stripe by infrared near-field imaging (inset of Fig. 4), we collected spectra from ~20 nm spots at three representative positions. These measurements were performed under 15 mW of optical pump power. The first spectrum collected from the insulating region (1) is dominated by a resonance at ~680 cm^{-1} characteristic of the monoclinic phonon mode of VO_2 which is known to be absent from the rutile phase [29–33]. Moving closer to the metallic stripe ($1 \rightarrow 3$ series), we observe a gradual increase in the electronic background. At position 3, the electronic background near the high frequency cutoff of our spectra is indistinguishable from that of the rutile phase. Nevertheless, the 680 cm^{-1} hallmark of the monoclinic phase persists throughout all spectra (1–3). For comparison, spectroscopy of the rutile metallic response acquired at the same location at a later stage of the phase transition (20 mW pump power) is also displayed (dashed red line). The 680 cm^{-1} phonon feature is not present in this latter spectrum, attesting to a complete transition into the rutile phase. We remark that the monoclinic metallic islands spontaneously appear across the sample and eventually evolve into metallic stripes. It is therefore unlikely that the nucleation of these initial metallic domains is governed by defects or surface contaminations. Nevertheless, defects smaller than the spatial resolution of our apparatus may play a role in triggering the metallic nucleation.

Our nanoimaging and nanospectroscopy experiments suggest the MIT of strained VO_2 films proceeds by three distinct stages [illustrated in Fig. 1(a)]. At the initial stage of the phase transition (exhibited by our 15 mW pump power measurements), sparse metallic nucleation occurs without an associated structural transition; this behavior is consistent with Mott physics [15,34–36]. At advanced stages of the phase transition (20 mW pump power, i.e., $T \simeq 340$ K), the formation of corrugated morphology and the monoclinic-to-rutile structural phase transition stabilize the network of metallic stripes, establishing a highly anisotropic electronic state in strained films. Finally, upon the transition finale (≥ 25 mW, ≥ 370 K), the film becomes a uniform rutile metal and exhibits a near-isotropic far-field response.

The infrared near-field imaging and spectroscopy measurements reported here uncover a novel aspect in the mesoscopic properties of VO_2 which proceeds beyond any single-phase description, offering new insights towards understanding the relationship between T_c, optical anisotropy, and strain in this prototypical transition metal oxide film. Providing VO_2 as a case study, here we have demonstrated the unique abilities of infrared near-field imaging and nano-FTIR to resolve and disentangle both structural and electronic phenomena, a crucial requirement for the future advances in the studies of phase transition in complex, phase separated materials [6,37,38]. As a side remark, we mention possible utility of the periodic stripe pattern revealed by our measurements. This pattern that can be tuned by temperature and light illumination and is also controlled by the sample thickness will produce diffraction characteristics in visible-IR frequencies that can augment current thermo- and electrochromic applications of VO_2.

D. N. B. acknowledges support from ARO. Development of nano-optics capabilities at UCSD is supported by DOE-BES. R. D. A. acknowledges support from DOE-BES under Grant No. DE-FG02-09ER46643. M. W. thanks the Alexander von Humboldt Foundation for financial support. E. A. acknowledges support from Fundação para a Ciência e a Tecnologia, Portugal, through a doctoral degree fellowship (No. SFRH/BD/47847/2008). S. K., J. L., and S. A. W. are grateful for the support from the Nanoelectronics Research Initiative (NRI) and VMEC.

*dbasov@physics.ucsd.edu

[1] J. Locquet, J. Perret, and J. Fompeyrine, Nature (London) **394**, 453 (1998).
[2] J. Wang, J. B. Neaton, H. Zheng, V. Nagarajan, S. B. Ogale, B. Liu, D. Viehland, V. Vaithyanathan, D. G. Schlom, U. V. Waghmare, N. A. Spaldin, K. M. Rabe, M. Wuttig, and R. Ramesh, Science **299**, 1719 (2003).
[3] N. Levy, S. A. Burke, K. L. Meaker, M. Panlasigui, A. Zettl, F. Guinea, A. H. Castro Neto, and M. F. Crommie, Science **329**, 544 (2010).
[4] N. Bowden, S. Brittain, and A. Evans, Nature (London) **393**, 146 (1998).
[5] V. Lyahovitskaya, Y. Feldman, I. Zon, E. Wachtel, I. Lubomirsky, and A. L. Roytburd, Adv. Mater. **17**, 1956 (2005).
[6] T. Z. Ward, J. D. Budai, Z. Gai, J. Z. Tischler, L. Yin, and J. Shen, Nat. Phys. **5**, 885 (2009).
[7] K. Ahn, T. Lookman, and A. Bishop, Nature (London) **428**, 401 (2004).
[8] B. Spivak and S. A. Kivelson, Ann. Phys. (Amsterdam) **321**, 2071 (2006).
[9] F. J. Morin, Phys. Rev. Lett. **3**, 34 (1959).
[10] J. B. Goodenough, J. Solid State Chem. **3**, 490 (1971).
[11] C. Everhart and J. MacChesney, J. Appl. Phys. **39**, 2872 (1968).
[12] J. Lu, K. G. West, and S. A. Wolf, Appl. Phys. Lett. **93**, 262107 (2008).
[13] S. Kittiwatanakul, J. Lu, and S. A. Wolf, Appl. Phys. Express **4**, 091104 (2011).
[14] V. Eyert, Ann. Phys. (Berlin) **11**, 650 (2002).
[15] B. Lazarovits, K. Kim, K. Haule, and G. Kotliar, Phys. Rev. B **81**, 115117 (2010).
[16] S. Biermann, A. Poteryaev, A. I. Lichtenstein, and A. Georges, Phys. Rev. Lett. **94**, 026404 (2005).
[17] A. Huber, A. Ziegler, T. Kck, and R. Hillenbrand, Nat. Nanotechnol. **4**, 153 (2009).
[18] D. Bonnell, D. Basov, M. Bode, U. Diebold, S. Kalinin, V. Madhavan, L. Novotny, M. Salmeron, U. Schwarz, and P. Weiss, Rev. Mod. Phys. **84**, 1343 (2012).

[19] J. M. Atkin, S. Berweger, A. C. Jones, and M. B. Raschke, Adv. Phys. **61**, 745 (2012).

[20] See Supplemental Material at http://link.aps.org/supplemental/10.1103/PhysRevLett.111.096602 for additional details on the methods and techniques we used in this Letter.

[21] S. Amarie, P. Zaslansky, Y. Kajihara, E. Griesshaber, W. W. Schmahl, and F. Keilmann, Beilstein J. Nanotechnol. **3**, 312 (2012).

[22] F. Keilmann and S. Amarie, J. Infrared Millimeter Terahertz Waves **33**, 479 (2012).

[23] E. Abreu, M. Liu, J. Lu, K. G. West, S. Kittiwatanakul, W. Yin, S. A. Wolf, and R. D. Averitt, New J. Phys. **14**, 083026 (2012).

[24] J. Wu, Q. Gu, B. S. Guiton, N. P. De Leon, L. Ouyang, and H. Park, Nano Lett. **6**, 2313 (2006).

[25] J. Cao, E. Ertekin, V. Srinivasan, W. Fan, S. Huang, H. Zheng, J. W. L. Yim, D. R. Khanal, D. F. Ogletree, J. C. Grossman, and J. Wu, Nat. Nanotechnol. **4**, 732 (2009).

[26] A. C. Jones, S. Berweger, J. Wei, D. Cobden, and M. B. Raschke, Nano Lett. **10**, 1574 (2010).

[27] A. Tselev, V. Meunier, E. Strelcov, W. A. Shelton, I. A. Lukyanchuk, K. Jones, R. Proksch, A. Kolmakov, and S. V. Kalinin, ACS Nano **4**, 4412 (2010).

[28] D. Kucharczyk and T. Niklewski, J. Appl. Crystallogr. **12**, 370 (1979).

[29] A. S. Barker, Jr., H. Verleur, and H. Guggenheim, Phys. Rev. Lett. **17**, 1286 (1966).

[30] A. Heinrich, E. I. Terukov, W. Reichelt, H. Wagner, and H. Oppermann, Phys. Status Solidi (a) **72**, K61 (1982).

[31] In raw IR reflectance or raw near-field IR scattering data, the apparent width of the phonon feature is determined by the difference between the longitudinal (ω_{LO}) and transverse (ω_{TO}) frequencies. This apparent width can exceed several hundred wave numbers and is ultimately governed by the oscillator strength of the phonon resonance proportional to ω_{LO}-ω_{TO} (see Refs. [29,30]). The genuine width of the phonon mode as a rule is much smaller and can only be estimated from the analysis of the optical constants governing reflectance or scattering data.

[32] M. M. Qazilbash, M. Brehm, G. O. Andreev, A. Frenzel, P. C. Ho, B.-G. Chae, B.-J. Kim, S. J. Yun, H.-T. Kim, A. V. Balatsky, O. G. Shpyrko, M. B. Maple, F. Keilmann, and D. N. Basov, Phys. Rev. B **79**, 075107 (2009).

[33] T. J. Huffman, P. Xu, M. M. Qazilbash, E. J. Walter, H. Krakauer, J. Wei, D. H. Cobden, H. A. Bechtel, M. C. Martin, G. L. Carr, and D. N. Basov, Phys. Rev. B **87**, 115121 (2013).

[34] M. M. Qazilbash, M. Brehm, B.-G. Chae, P. C. Ho, G. O. Andreev, B.-J. Kim, S. J. Yun, A. V. Balatsky, M. B. Maple, F. Keilmann, H.-T. Kim, and D. N. Basov, Science **318**, 1750 (2007).

[35] H.-T. Kim, Y. W. Lee, B.-J. Kim, B.-G. Chae, S. J. Yun, K.-Y. Kang, K.-J. Han, K.-J. Yee, and Y.-S. Lim, Phys. Rev. Lett. **97**, 266401 (2006).

[36] Z. Tao, T.-R. T. Han, S. D. Mahanti, P. M. Duxbury, F. Yuan, C.-Y. Ruan, K. Wang, and J. Wu, Phys. Rev. Lett. **109**, 166406 (2012).

[37] E. Dagotto, T. Hotta, and A. Moreo, Phys. Rep. **344**, 1 (2001).

[38] S. A. Kivelson, I. P. Bindloss, V. Oganesyan, J. M. Tranquada, A. Kapitulnik, and C. Howald, Rev. Mod. Phys. **75**, 1201 (2003).

Supplementary material for anisotropic electronic state via spontaneous phase separation in strained Vanadium Dioxide films

Mengkun Liu[1], Martin Wagner[1], Elsa Abreu[2], Salinporn Kittiwatanakul[3], Alexander McLeod[1], Zhe Fei[1], Michael Goldflam[1], Siyuan Dai[1], Michael Fogler [1], Jiwei Lu[4], Stuart A. Wolf[3,4], Richard D. Averitt[2], D. N. Basov[1*]

1. Department of Physics, The University of California at San Diego, La Jolla, California 92093, USA
2. Department of Physics, Boston University, Boston, Massachusetts 02215, USA.
3. Department of Physics, University of Virginia, Charlottesville, Virginia 22904, USA.
4. Department of Materials Science and Engineering, University of Virginia, Charlottesville, Virginia 22904, USA.

Near-field infrared microscopy. Infrared scattering-type scanning near-field optical microscopy (s-SNOM) is an optical antenna-based near-field scattering technique. This instrument is a hybrid of an atomic force microscope (AFM) and infrared lasers [1]. S-SNOM naturally provides exquisite optical imaging and spectroscopy capabilities with a spatial resolution limited only by the apex radius of the AFM tip (~20nm in our case). In a typical setup, a broadband or CW laser beam is focused onto a metalized AFM tip, and the back-scattered signal (S_n) is demodulated at integral harmonics n=2, 3, … of the tip's tapping frequency. The higher harmonic signals (S_2-S_3) reflect the strength of near-field coupling between the AFM tip and the sample surface, thus conveying information about the local dielectric function [2,3].

Near-field infrared spectroscopy. In order to perform nano-Fourier transform infrared spectroscopy (nano-FTIR), broadband IR pulses from a 40 MHz Er-doped fiber laser are used as a coherent light source [4]. The Mid-IR probe pulses are generated via difference frequency

generation (DFG) in a GaSe crystal with <100 fs pulse duration. The center frequency of the near-field probe spectrum is tunable from ~800 cm^{-1} to ~2200 cm^{-1} with a typical bandwidth of ~250 cm^{-1}. Spectra of the amplitude and phase of tip-scattered fields are obtained via Michelson interferometric detection, analogous to conventional Fourier transform spectroscopy. For the purpose of imaging, the reference beam of the interferogram is blocked and the near-field scattering signal is spectrally integrated. Specifically, Fig. 2 and Fig. 3 display images of the S_3 near-field signal integrated within a 900~1300 cm^{-1} spectral range. The infrared near-field spectroscopy measurements presented in Fig. 4 are nano-FTIR S_2 spectra in the range 600-1000 cm^{-1}, which cover the spectroscopic signature of monoclinic optical phonon mode at ~680 cm^{-1}. The image in the inset of Fig. 4 displays the integrated S_2 signal obtained with the same probing spectrum as the Fig. 4 nano-FTIR data.

The 1.56 μm near-IR pump pulses were also produced at 40 MHz by our Er-doped fiber laser. Pump power was controlled with a neutral density filter with a peak power of ~25 mW. In this report, the near-IR pump can be regarded as a convenient thermal source targeting only the absorbing VO_2 film without directly heating the substrate. This minimizes thermal drift and provides better instrumental stability than heating by means of a conventional temperature stage.

Thickness dependent near-field study. We performed a series of near-field (S_3) imaging experiments on VO_2 samples on $[110]_R$ TiO_2 substrate with different sample thickness (Fig. S1). It is clear that in the same temperature range the periodicity of the stripes (D) increases with increasing film thickness. This is a result of the subtle balance/competition between the domain interfacial energy and the elastic energy. The former favors domains with longer period D, so that there are fewer interfaces. The corresponding energy per unit length scales as 1/D. The elastic energy favors closer spaced domains since the corresponding elastic energy per unit

length scales as D. There is an optimal periodicity where the sum of these two energy terms (per unit volume), A(D) +B(1/D), is minimized, which yields $D_{optimal}=\sqrt{B/A}$. Since thinner films experience higher elastic energy due to the substrate induced epitaxial strain (larger A), the periodicity is smaller compared to thicker films (smaller D). Similar thickness-periodicity relationship has also been studied in the case of VO_2 nano-beams (see a more rigorous energy expression in Ref. [5]). In the case of VO_2 films that we investigated in this work the stripe state is not impacted by geometric restriction and dimensional confinement of nano-beams. The stripes in our films are a direct product of crystallography and strain environment.

Samples. The VO_2 films studied in this report are deposited on $[110]_R$ TiO_2 substrates (1 cm × 1 cm) by temperature-optimized sputtering using the reactive bias ion beam deposition technique in an Ar+O_2 gas mixture. High quality films with varied thicknesses (53, 100, 200, 300 nm) were investigated, revealing consistently anisotropic THz and DC conductivity. Due to the lattice mismatch between TiO_2 and VO_2, there is a 1-2 % tensile strain along c_R axis in these films. In order to clearly expose the sample's morphological changes by AFM, we presented results for the thickest film (300nm) on $[110]_R$ TiO_2 substrate. These latter films show *no cracks* over the entire sample surface (1cm x 1cm).

THz spectroscopy. The THz conductivity of the films was measured by time domain spectroscopy (THz-TDS) with a THz beam diameter of ~3 mm (FWHM). Transient THz pulses are generated and detected by electro-optic techniques using a ZnTe crystal and a regenerative amplifier producing 35 fs, 3.5 mJ near-IR pulses at 800nm. With polarization-sensitive THz-TDS experiments we measured far-IR conductivity in a non-contact manner, spatially averaged over the beam diameter (3mm).

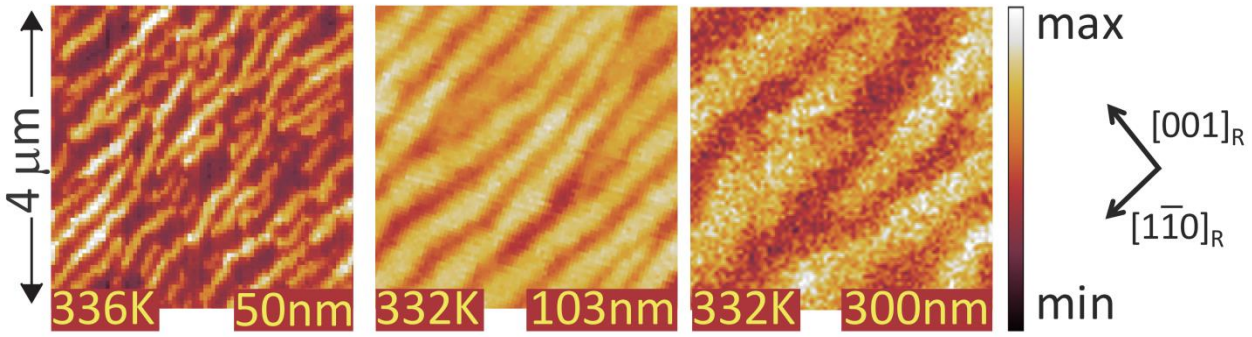

Fig. S1: Near-field imaging (S_3) of VO_2 films with different film thickness on $[110]_R$ TiO_2 substrates.

References:

[1] H. U. Yang, E. Hebestreit, E. E. Josberger, and M. B. Raschke, Review of Scientific Instruments **84**, 023701 (2013).

[2] A. C. Jones, S. Berweger, J. Wei, D. Cobden, and M. B. Raschke, Nano Letters **10**, 1574 (2010).

[3] A. Huber, A. Ziegler, T. Köck, and R. Hillenbrand, Nature Nanotechnology **4**, 153 (2009).

[4] F. Keilmann and S. Amarie, Journal of Infrared, Millimeter, and Terahertz Waves **33**, 479 (2012).

[5] J. Wu, Q. Gu, B. S. Guiton, N. P. De Leon, L. Ouyang, and H. Park, Nano Letters **6**, 2313 (2006).